

A De-Convolution Technique used for NDT in X-ray & CT

K. Chui¹

Image Enhancement Technology Ltd¹
8 Gilbey Close, Ickenham,
Uxbridge, Middlesex, UB10 8TD, UK.

ming-chui@iet.org.uk

S. Chui²

Worcester Acute Hospital NHS Trust²
Radiology Department,
Woodrow Drive, South Woodrow,
Redditch, Worcester B98 7UB UK.

shyrchui@netscape.net

A. Wride¹

andrew.wride@lineone.net

D. Stanfield¹

dbs@iet.org.uk

ABSTRACT -

A De-Convolution Technique for the detection and enhancement of image edge-profiles to the sub-pixel accuracy without any trade-off loss has been found. Enhancement via the removal of the penumbral-spread effect within a zoomed space is carried out empirically via sub-pixel transfers and under the spatial bandwidth control of a global Line-Spread-Function that no ambiguity is introduced. Phantom calibrations and field NDT examples in X-ray and CT were used to demonstrate its merits i.e. in both the improved spatial resolution in image and the improved accuracy to the sub-pixel level in measurements. Clearer diagnosis in image and accurate measurements have been achieved by using this methodology, which may lead to the finding of a definitive method used in Quantitative Radiology in NDT. Its key application is in the accurate quantitative assessment or monitoring of fracture(s) or minute defect(s) under any mechanical stress or strain.

Keywords -

X-ray, CT, Image, Enhancement, Deconvolution, Technique, NDT

Background -

(1) History of the Problem - Blurred image-edges caused by the 'Penumbral-Spread Effect' have existed since the discovery of X-ray (that led to its Radiography) in 1895. Even in Computed Tomography (CT), the combined effect of the size of the energy source and/or the size of the detector(s) still result in the 'Penumbral Spread' problem.

(2) Previous Work -

(a) The hardware solution to the problem involves the collimation of the photon beam, which reduces the dose efficiency and results in an increase in image noise (Ref. [2]).

(b) Prior related works

In 1989, Alperin worked on the "Automatic Analysis of Coronary Lesions from Cineangiograms using Vessel Tracking and Iterative De-Convolution Technique [3]. Charland recovered the Line Spread Function of Radiation Detector using the De-Convolution Technique [4]. Marsudi used an edge model derived by convolving a signal with energy filters to extract 2D edge feature to sub-pixel accuracy [5]. Smith used two-dimensional De-Convolution Technique to remove the blurred edges for small spatial measurement in X-ray Radiography [6]. Keller used the upper and lower CT contrast threshold to determine the edge-profile(s) for the outlining of its contour [7]. Chui used the De-Convolution Technique

to measure the slice-thickness in MR scan [8]. Numerous medical applications by CAD based on the De-Convolution Technique have also been realized by Chui et.al. [9].

None of the above methods involve entering the magnified sub-pixel domain to improve the spatial resolution. In fact, they all operate in the pixel domain and therefore have the minimum experimental tolerance of ± 1 pixel, which are two pixels. From the CT phantom calibration detailed later in this paper; the mean penumbral-spread effect was measured to be in the range of 2.0 – 2.4 pixels. It is, therefore practically limited in the detection or any further enhancement of an effect, which is at the same magnitude as the experimental error. Therefore, the effect can only be detected and enhanced by a methodology, which is sufficiently accurate and implemented within a magnified sub-pixel domain.

(3) The Solution detailed in this Study -

In each image matrix, there are two components of spatial resolution. The first one is the spatial resolution defined by the pixel size, or more specifically, by the reciprocal of the distance (i.e. in number of pixel modulation per distance) between adjacent pixels. The maximum of which, is the diagonal spatial resolution at forty-five degree angle. Its vector direction is along the edge-profile of contrast. The second component of spatial resolution is orthogonal to the first one. This second component of spatial resolution is most affected by the Penumbral-Spread Effect. Nevertheless, it is often the second component of spatial resolution plus the signal-to-noise (e.g. the voxel size) consideration that determines the selection of the first. In Physics, one may independently improve or change the property of one orthogonal vector without affecting the other vector orthogonal to it.

The main purpose of this study is to improve the second component of spatial resolution by the elimination or the correction of the Penumbral-Spread Effect.

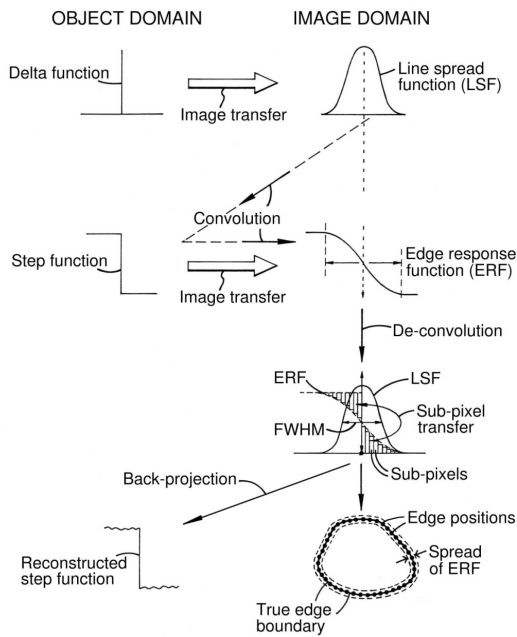
Our current solution -

Recently, using the processing power of modern CPUs, an innovative software solution to the problem without any trade-off increase in image noise has been founded. It is a post-processing De-Convolution Technique for the detection, definition and enhancement of image edge-profiles. Sub-pixel sampling at the Nyquist frequency was used to preserve the spatial resolution of the first component. The detection of true edge-positions and enhancement of edge-profiles via sub-pixel transfer were carried out in the magnified sub-pixel domain to improve the spatial resolution of the second component, which is most affected by the Penumbral-Spread Effect.

Enhancement is carried out in a magnified space with magnification factor of 3, 5, 7, or 9. The upper limit of magnification factor of 9 was used due to the $1/10^{\text{th}}$ pixel of experimental error at 1% low-contrast noise limitation (refer to Evaluation & Results section). Within this zoomed span of 3 to 9, the higher the magnification factor, the clearer is the enhanced image obtained, as both the Penumbral-Spread Effect and the Pixelization Effect are overcome at the same time by the processing. By solving this previously 'unsolvable' century-old problem without any trade-off loss, numerous important applications may now be realized.

The Principle of the De-Convolution Technique -

Figure 1



Due to the size of the energy source, detector size for some imagers and other second order factors such as contrast level, noise spike, overshoots, and local partial volume effects, a Delta Function in the Object Domain cannot be reproduced in the Image Domain. Instead, a “local” Line Spread Function (LSF) of a specific shape is obtained. Similarly, a specific-shaped “local” `blurred’ Edge Response Function (ERF) is obtained from the Step Function (SF) of an object (Figure 1). This specific-shaped `blurred’ ERF varies from edge-position to edge-position. The blurred feature may be described as the “Blooming Effect” of varying windows settings, which is mainly caused by the above `Penumbral Spread’ Problem. Mathematically, the ERF can be derived by the Convolution of the LSF with the SF (Figure 1 & the Mathematical Model). Experimentally; we may derive the “local” LSF from the ERF by the De-Convolution Process

using a Running Filter Technique (Figure 1 & Mathematical Model). By overlaying the "local" LSF over its specific-shaped `blurred’ ERF, the true edge position is calculated from the mid-point of the full-width-half-maximum (FWHM) to sub-pixel accuracy (Figures 1, 2 & 3). Sub-pixels from the low-contrast side of the edge can then be transferred over to the higher-contrast side of the edge to restore, empirically, the original SF feature and to enhance the image-edge without any increase in image noise. The processes of the De-Convolution and enhancement are both carried out under the strict spatial bandwidth controls of a global LSF that no ambiguity is introduced.

Figure 2 - Example: LSF derived from ERF

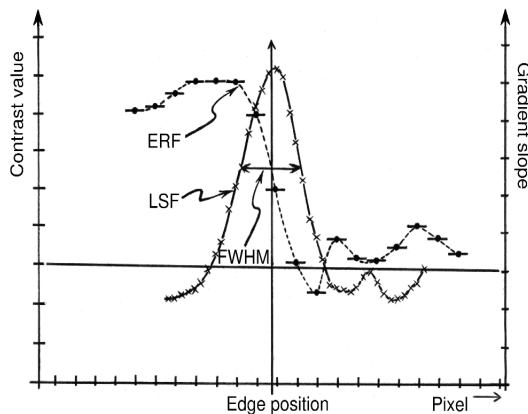
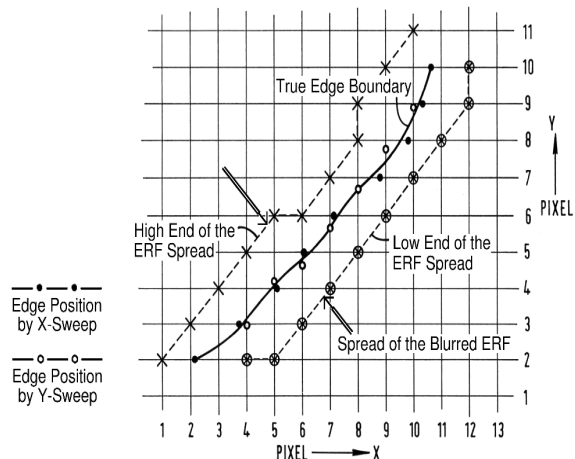


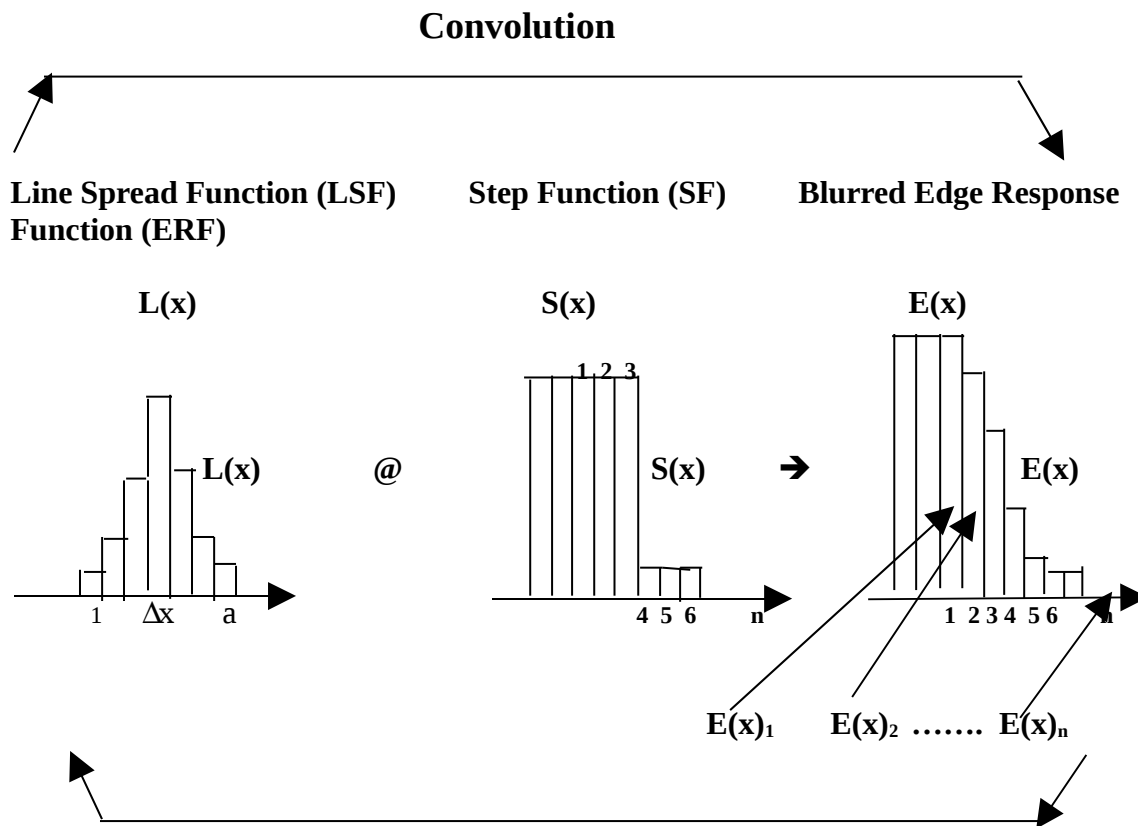
Figure 3 - Example: Magnified section



Enhancement is carried out by the empirical transfer of sub-pixels from the low-end of the edge over to the high-end to restore the high-resolution feature at each edge position of the edge-profile without any trade-off loss, which may result in any increase in image-noises. Both the De-Convolution and Reconstruction processes are carried out under the strict spatial bandwidth controls of a global LSF so that no ambiguity such as the gradual slope profile is detected.

All the edge-detection, enhancement and operational functionalities are incorporated into a Computer Aided Detection (CAD) software package via a DICOM toolkit.

Mathematical Model - The mathematical models of the Convolution and then the De-Convolution are described as follows:-



Mathematical Model -

Convolution -

At Point 1: $\sum_{1}^{a} L(x) \Delta x = E(x)_1$
 “ “ “ “ “ “

At Point n: $\sum_{1}^{a} L(x) \Delta x - \sum_{a-(n-1)}^{a} L(x) \Delta x = E(x)_n$ where n = 1, 2, 3, ...or n.

De-Convolution -

Between Point 1 → Point 2:

$E(x)_1 - E(x)_2 = \sum_{a-1}^{a} L(x) \Delta x = \{L(x)_a - L(x)_{(a-1)}\} \Delta x$

or $\{E(x)_1 - E(x)_2\} / \Delta x = L(x)_a - L(x)_{(a-1)}$

Leading to:- Between Point (n-1) → Point n:

$\{E(x)_{n-1} - E(x)_n\} / \Delta x = L(x)_n - L(x)_{(n-1)}$ where n = 1, 2, 3, ...or n.

Evaluation and Results -

Phantom of contrast edge was scanner examined. Optimal accuracy and sensitivity of the methodology could be achieved via the optimization of parameters used. Nyquist sub-pixel sampling criteria were imposed to ensure the full extraction of the 'cut-off' spatial resolution of the first type. In *Figure 2 – Example: LSF derived from ERF*, the 'step-shape' feature of the pixel data of the Edge Response Function (ERF) of the contrast edge was reduced to the 'smooth' feature of the derived LSF due to the smoothing effect of the Running Filter. The length of the Running Filter of the De-Convolution could be lengthened (increasing smoothing to reduce noise) or shortened (to increase the sensitivity). Further averaging is made by calculating the mid-point of the full-width-half-maximum (FWHM) of the LSF to achieve the sub-pixel accuracy (*Figure 2* illustrates the intercept of the normal vector of the mid-point of FWHM with the X-axis).

In *Figure 3* – several edge-positions via the X-sweep (solid black circles) and Y-sweep (white rings) were sampled to form the edge-profile as indicated by the solid black line through the edge-positions. The two arrows indicate the extent of the "blurring" at the original ERFs., which was measured to be 2.4 pixels in average. The smooth edge-profile indicated the accuracy to the sub-pixel level as well as the feature of the edge-profile 'after' its enhancement. It is quite apparent that the effect of enhancement 'can only be visualized' or 'with properties accurately measured' within the magnified sub-pixel space domain.

2) Calibrations - A New York Catphan 500 was examined using Single Slice helical CT using technique factors of 120kVp, 300mA, 4 secs., 10mm slice.

Distance, area, and volume calibrations, high & low contrast resolutions, and processing time were studied:

(i) Distance, Area and Volume Measurements

Distance – At high-contrast & 1% low-contrast edge, accurate to $1/50^{\text{th}}$ of a pixel in $(\Delta)r$ (i.e. $(\Delta)r$ in $(\Delta)r/r$); and,

Area/Volume – At high-contrast & 1% low-contrast edge, accurate to $1/18^{\text{th}}$ & $1/10^{\text{th}}$ of a pixel in $(\Delta)r$ (i.e. $2(\pi)r(\Delta)r/(\pi)r^2$ or $(\Delta)(\text{area}) = 2(\pi)r(\Delta)r$)

(Volume = Area x Slice-thickness).

(ii) High Contrast Resolution

Mean Modulation Transfer Function (MTF) at the high contrast Teflon edge were improved from 3.38 lp/cm to 7.75, 8.94, 9.61 and 10.04 lp/cm at 50% normalized modulation level and from 5.83 lp/cm to 11.89, 13.90, 15.03, and 15.75 lp/cm at 10% normalized modulation level respectively after 3x, 5x, 7x and 9x magnification and enhancement. The calculations were made by the method of P. Judy [10].

(iii) Low-Contrast Resolution

(a) Resolved 1% low contrast rod down to 3mm at 50mA;4 secs;120 kVp;5mm slice; or

(b) Well-resolved 0.3% low contrast to 2mm rod at 300mA, 120kVp;4 secs;10mm slice.

(iv) Processing Time

At 3x, 5x, 7x, 9x magnification of Region of Interest (ROI) (i.e. 107x107, 64x64, 46x46, & 36x36 matrix respectively), it took 4.67, 0.98, 0.43, 0.29 seconds by a 600 MHz CPU and 1.17, 0.25, 0.11, and 0.07 seconds by a 2.4 GHz CPU respectively.

(v) Limitation

The De-Convolution Technique works well at the medium to high-contrast edges but less well at the low-contrast edges, particularly in a noisy image. - The large noise grains of a noisy image will cause the 'zig-zag' feature at the edge-profile.

There are three possible ways to overcome this limitation:-

- (1) In NDT, use higher tube potential, kVp, to produce the more penetrating X-ray for a better signal-to-noise radiography image;
- (2) Use Subtraction X-ray Technique to remove the background noise grains; or,
- (3) Bring in a noise filter. (the use of a noise filter may smoothen out some useful

high spatial frequency information).

Therefore only Options (1) & (2) are recommended at this stage.

3) Field-Examples -

Phantom and non-medical field-examples were illustrated:

(A) X-ray, In-Plane -

(i) wire-thickness (59kVp, 151mA)-, $t(\text{mechanically})=0.54\text{mm}$; $t(\text{software})=0.565\text{mm}$;

Diff.=+4.62 % (Figures 7-9).

(ii) Emulated weld-cracks* (145kVp;1mA)– barely visible enhanced to clearly visible, maximum-width of main crack, $w=0.36\text{mm}$ (Figures 13-15).

(B) X-ray, Between-Planes -

(i) wire-thickness(59kVp, 151mA)-, $t(\text{mechanically})=0.54\text{mm}$; $t(\text{software})=0.548\text{mm}$;

Diff.=+1.48 %. (Images 'before' and 'after' 9x ROI (Region of Interest) enhancement are illustrated in Figures 7-9).

(ii) Guide wire in Guide-Wire & Coins Phantom (55kVp;153mA)(Figures 4-6), manufacturer's specification, $d=0.89\text{mm}$, measured value, $d'=0.91\text{mm}$; Error=+2.25%; and,

(iii) Wire-pairs* (145kVp;1mA)(Figures 10-12); wire-pairs thickness (manufacturer's spec.)=0.16mm; measured value=0.166mm. Error=+3.75%.

(C) Digitally scanned CT scan image of fiberglass section (120kVp, 28mA) image was analyzed. Barely visible defects were enhanced to clearly visible (Figures 16-18).

(D) 'bubble' or 'defect' within a jet turbine blade is enhanced. Images of 'before' and 'after' are shown in the Slide-Set 3 on NDT. Figure 19 was the original image of a X-ray image of 'bubble' trapped in a jet turbine blade by polychromatic X-ray. Figures 20 & 21 were the 'before' and 'after' images of 7xROI on the 'bubble' area.

[Note – monochromatic X-ray diffraction on the adjacent areas around the 'bubble' may illustrate the deformation of the crystal lattices under stress.]

.....
Two medical examples were illustrated:-

(E) This example showed an 'invisible' bone fracture enhanced to clearly 'visible' for diagnosis and accurate measurements. Figure 22 showed the original image of humerus fracture (at the tip-end of an elongated fracture) with ROI of a CT scan. Figures 23 & 24 were 7x ROI 'before' and 'after' enhancement. Figure 25 was the image with the annotation for measurement. Minute fracture gap = $1.35\pm 0.02\text{mm}$;

and,

(F) This CT example (64 rows data, technique factors: 135kVp; 420mA; 0.5mm slice-thickness; Exp. time=1s) showed the enhanced fractured thigh femur with an inserted intramedullary fixating nail. Intensity of streaking artifacts off the steel nail was considerably reduced by the selective enhancement of the high-contrast bone fractures over the medium-contrast streaking artifacts. This enabled the clearer diagnosis and accurate measurements of the minute fractures to be made. Figure 26 was the original image with ROI placed on the fractures with the inserted nail. Figures 27 & 28 were images of 'before' and 'after' enhancement. Figure 29 is the image with annotations for the measurements of: Fracture Gap 1 (bottom right)= $0.93\pm 0.01\text{mm}$; Fracture Gap 2 (bottom)= $0.52\pm 0.01\text{mm}$; & Fracture Gap 3 (right)= $0.63\pm 0.01\text{mm}$.

Conclusion –

The ERF-blurring or “penumbral-spread” can not be overcome by current digital enhancement as its true edge position is not located. But this deconvolution technique permits sensitive and accurate edge-profile detection and enhancement to overcome the century old

“penumbral-spread” problem without any trade-off loss, which may result in noise increase.

Invisible and barely visible minute fractures or effects were enhanced to clearly visible for accurate diagnosis and measurements for the quantitative assessment in various applications. For example, it is useful in:

- (1) to accurately monitor minute fractures or defects under mechanical stress or strain in non-medical applications; and,
- (2) to quantitatively assess the fracture bone healing progress in medical applications.

References -

- 1) K. Chui, *Imaging*. Patent No. GB 2 346 028 (05/Mar/2003), US Patent No.US6,928,182 (09/Aug/2005), & German Patent No. DE 699 22 983 T2 (29/Dec/2005).
- 2) K. Chui et. al. *Picture Quality of the High Resolution Option on CT*. Internal Report EMI (Medical), July, 1978, Hayes, Middlesex.
- 3) N. Alperin et. al. *Automatic Analysis of Coronary Lesions from Cineangiograms using Vessel Tracking and Iterative De-Convolution Techniques*. Proceedings of the Computers in Cardiology Meeting, US, Washington, IEEE Comp. Soc. Press, vol. Meeting 16, October 1989 (1989-10), pages 153-156.
- 4) P. Charland et. al. *The Use of De-Convolution and Total Least Squares in Recovering a Radiation Detector Line Spread Function*. Medical Physics, US, American Institute of Physics, New York, Vol. 25, No.2, February 1998 (1998-02): p152-160.
- 5) M. Kisword et. al. *2-D Edge Feature Extraction to Sub pixel Accuracy using Generalized Energy Approach*. Proceedings of The International Conference on EC3 – Energy, Computer Communication and Control Systems (Tencon), US, New York, IEEE, Vol.-, 2 August 1991 (1991-08-02), p344-348.
- 6) L. Smith. *Method and Apparatus for Measuring Small Spatial Dimensions of An Object*. US Patent No. 4,947,323 (07/Aug/1990).
- 7) J. Keller et. al. *Automatic Outlining of Regions on CT Scans*. Journal of Computer Assisted Tomography 5(2): 240-245, April, 1981.
- 8) K. Chui et. al. *Technical Note - Test Method for MR Image Slice Profile*. Journal of Computer Assisted Tomography, 9(6), 1150-1152, Nov/Dec. 1985. and UK Patent No. GB 2 155 187 (18/Sept/1985).
- 9) K. Chui et. al. *The Sensitive and Accurate De-Convolution Technique to Correct for the 'Penumbra-Spread Effect' in CT, MR, & DF*. Eur. Radiol. 2006, Feb.,16 (Suppl.): 287 [European Congress of Radiology-2006] and EPOS™-2006 B-652 [Search (top right) for "B-652"].
- 10) P. Judy. *The line spread function and modulation transfer function of a computed tomographic scanner*. Med. Phys. Vol. 3, No. 4, Jul/Aug 1976, p233-236.

Images – Figure 1 – the De-Convolution Technique; Figure 2 – LSF derived from ERF; Figure 3 – Magnified Section; Figure 4 – Original image of guide wire & coin phantom; Figure 5 – Guide wire 'before' enhancement; Figure 6 – 9x ROI – Guide wire 'after' enhancement; Figure 7 – Original image of components; Figure 8 – 9x ROI 'before' enhancement of components; Figure 9 – 9x ROI 'after' enhancement of components; Figure 10 – Original image of wire-pairs*; Figure 11 – 9xROI 'before' enhancement on wire-pairs*; Figure 12 – 9xROI 'after' enhancement on wire-pairs*; Figure 13 – Original image of emulated weld-cracks*; Figure 14 – 9xROI 'before' enhancement on emulated weld-cracks*; Figure 15 – 9xROI 'after' enhancement with annotation on emulated weld-cracks*; Figure 16 – Original image of CT photo of helicopter blade with ROI on defects; Figure 17 – 9xROI on defects 'before' enhancement; Figure 18 – 9xROI on defects 'after' enhancement; Figure 19 – Original image of 'bubble' in jet turbine blade; Figure 20 – 7xROI 'before' enhancement of the 'bubble' defect; Figure 21 – 7xROI 'after' enhancement of the 'bubble' defect; Figure 22 – Original CT image of 'invisible' humerus fracture; Figure 23 – 7xROI 'before' enhancement; Figure 24 – 7xROI 'after' enhancement; Figure 25 – Original image of fractured thigh femur with an inserted intramedullary fixating nail; Figure 26 – 7xROI 'before' enhancement; Figure 27 – 7xROI 'after' enhancement.

Acknowledgment – Image samples marked with* were sourced from TWI Ltd.

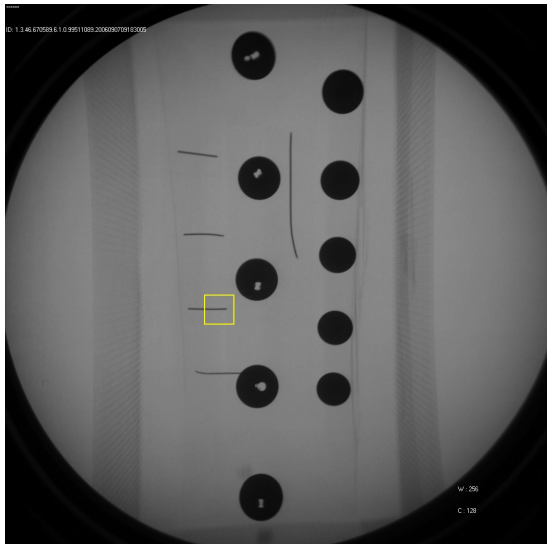


Figure 4: Original image of guide wire & coins with ROI.

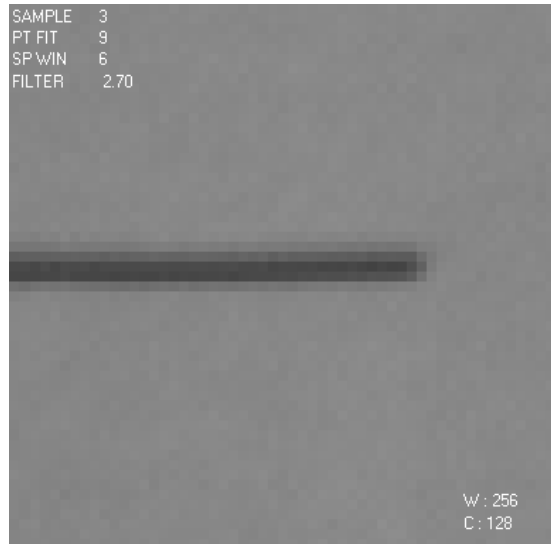


Figure 5: 9x ROI on guide wire 'before' enhancement.



Figure 6: 9x ROI on guide wire 'after' enhancement.

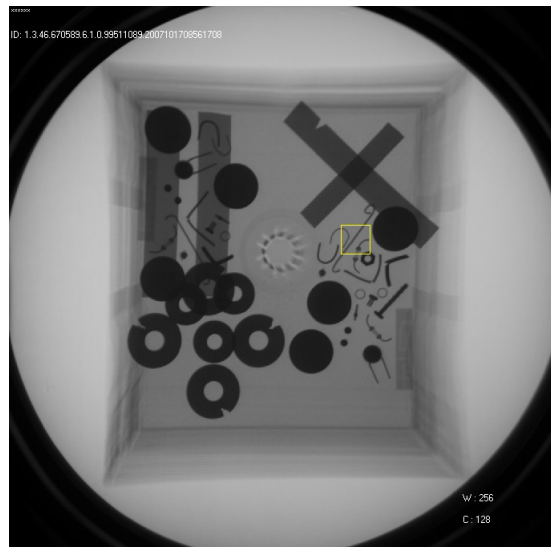


Figure 7: Original image of components with ROI.

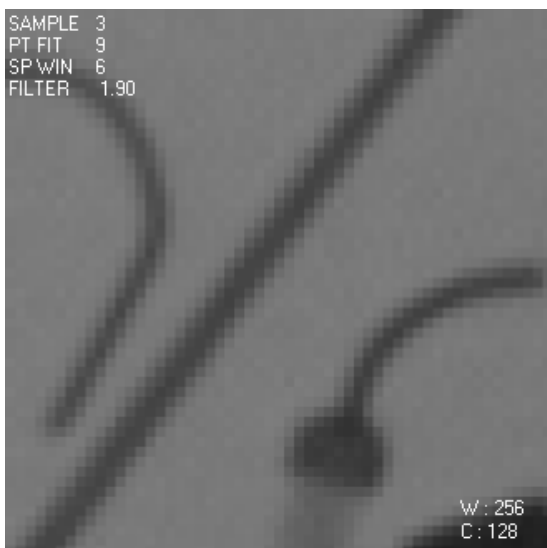


Figure 8: 9x ROI on components 'before' enhancement.

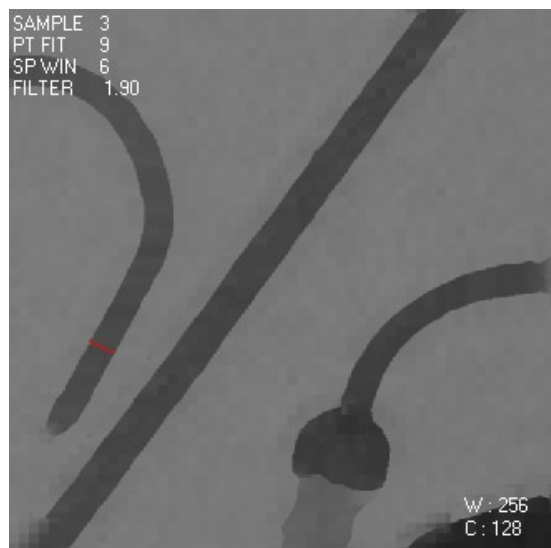


Figure 9: 9x ROI on components 'after' enhancement.

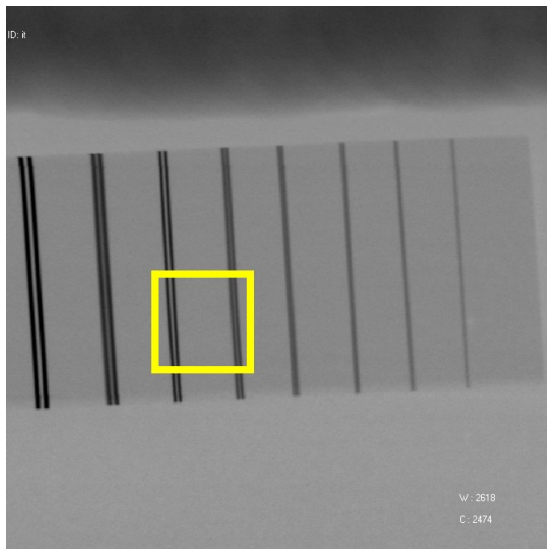


Figure 10: Original image of wire-pairs with ROI.

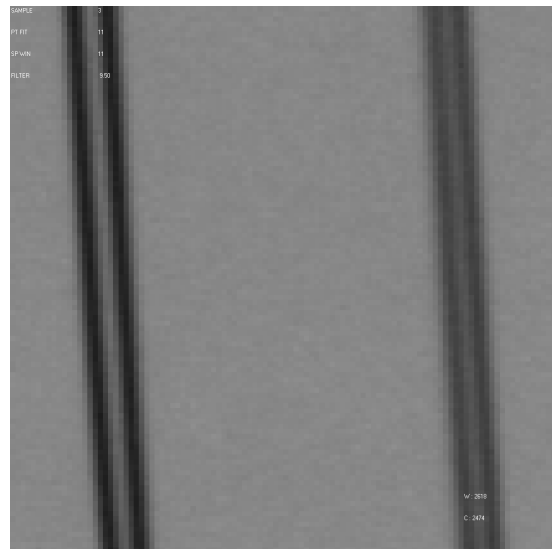


Figure 11: 9x ROI on wire-pairs 'before' enhancement.

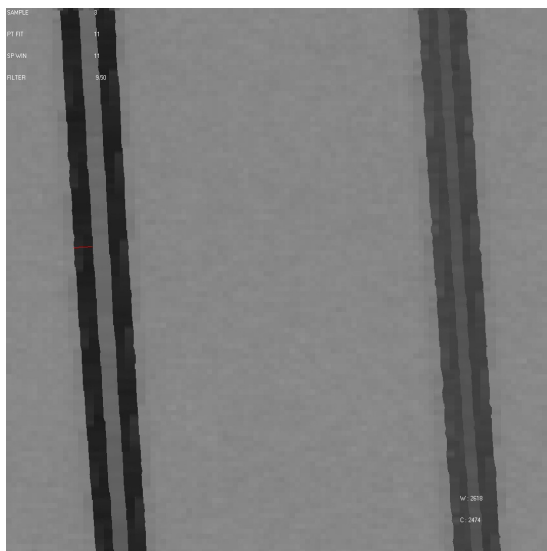


Figure 12: 9x ROI on wire-pairs 'after' enhancement.

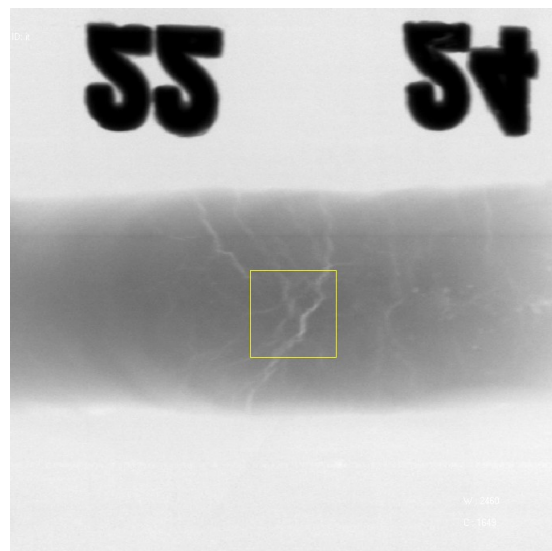


Figure 13: Original image on emulated weld-cracks.



Figure 14: 9x ROI on weld-cracks 'before' enhancement.

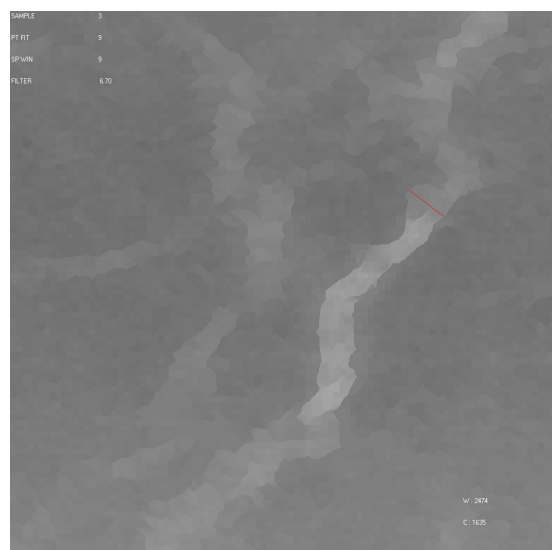


Figure 15: 9x ROI on weld-cracks 'after' enhancement.

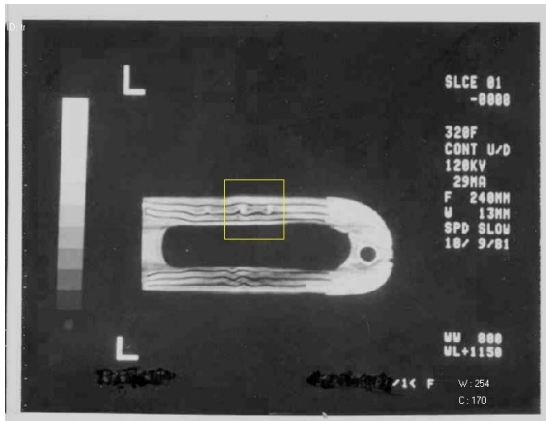


Figure 16: Original image of helicopter blade with ROI.

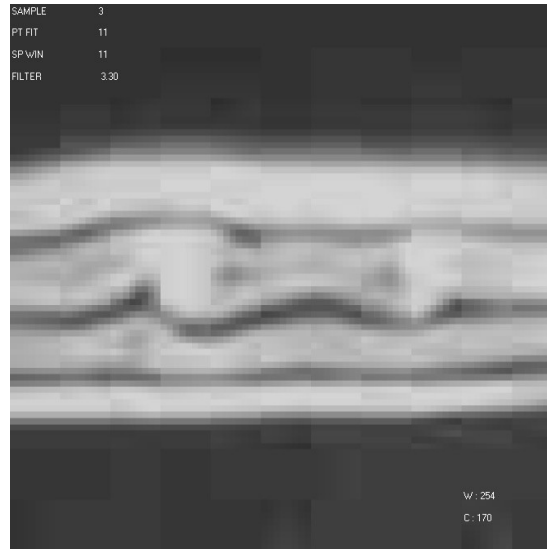


Figure 17: 5x ROI on fracture 'before' enhancement.

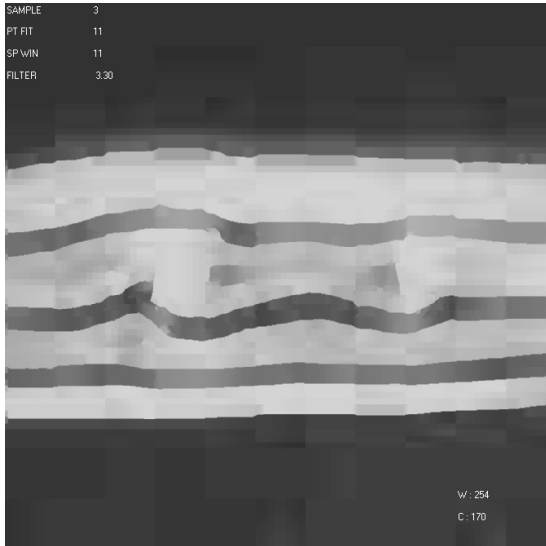


Figure 18: 5x ROI on fracture 'after' enhancement.

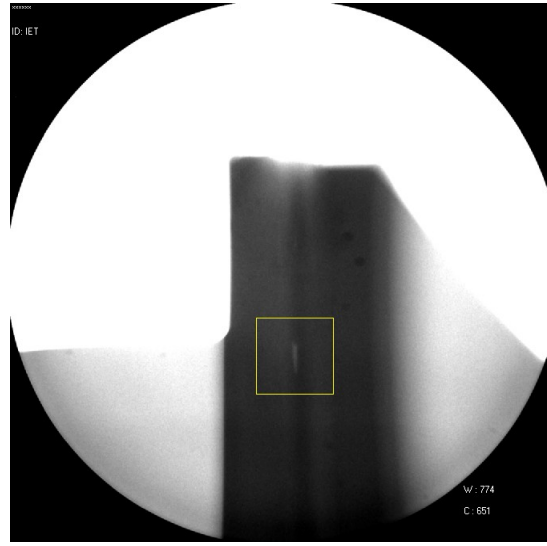


Figure 19: Original image of 'bubble' in jet turbine blade, with ROI.



Figure 20: 7x ROI of the 'bubble' defect 'before' enhancement.



Figure 21: 7x ROI of the 'bubble' defect 'after' enhancement.



Figure 22: Original image of humerus fracture with ROI.

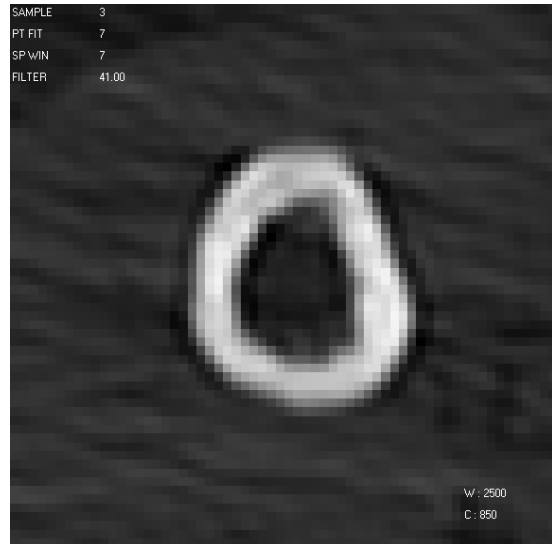


Figure 23: 7x ROI 'before' enhancement.

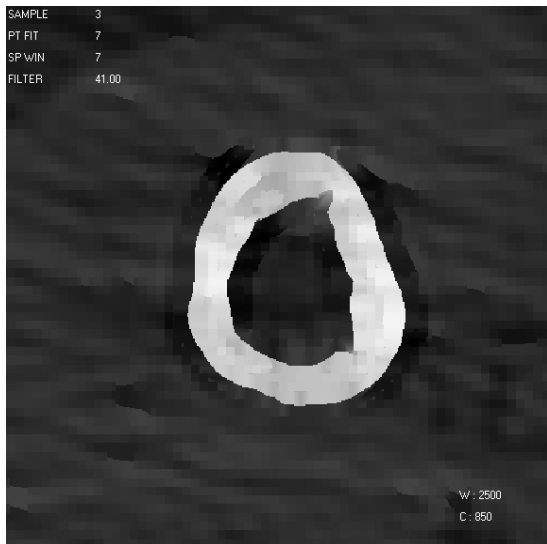


Figure 24: 7x ROI 'after' enhancement.

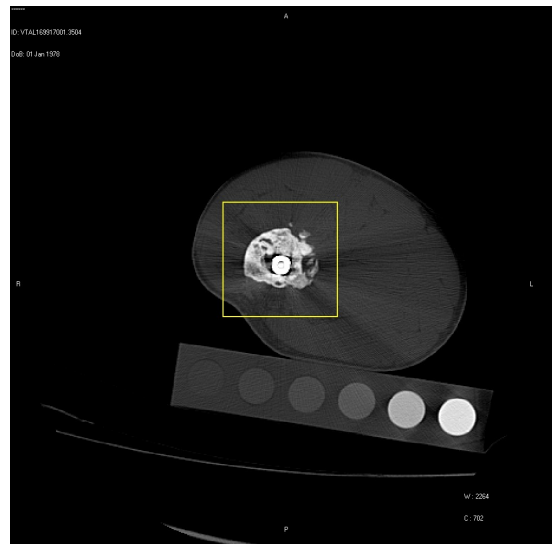


Figure 25: Original image of fractured thigh femur with an inserted intramedullary fixating nail.

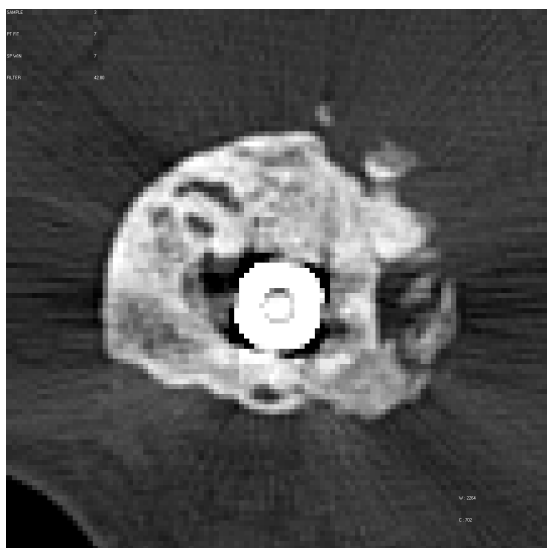


Figure 26: 7x ROI 'before' enhancement.

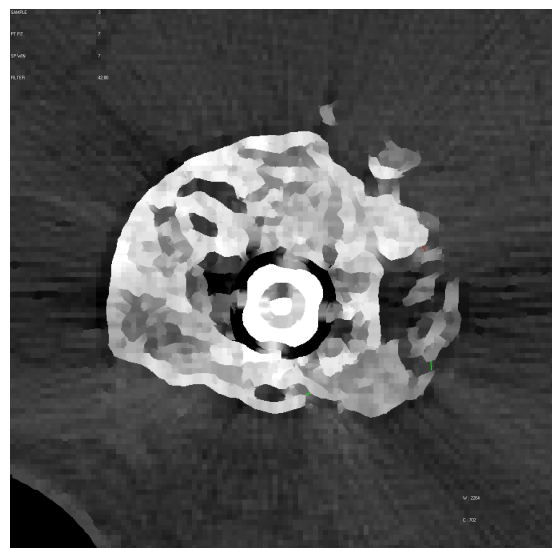


Figure 27: 7x ROI 'after' enhancement.